Flexible nanoporous activated carbon for adsorption of organics from industrial effluents

DOI:
10.1039/d1nr03242a

Document Version
Accepted author manuscript

Flexible nanoporous activated carbon for adsorption of organics from industrial effluents

Usama Zulfiqar [a], Nikolaos Kostoglou [b], Andrew G. Thomas [a], Claus Rebholz [a,c,*], Allan Matthews [a,*] and David J. Lewis [a,*]

[a] Department of Materials, University of Manchester, Oxford Road, Manchester M13 9PL, UK

[b] Department of Materials Science, Montanuniversität Leoben, 8700 Leoben, Austria

[c] Department of Mechanical and Manufacturing Engineering, University of Cyprus, 1678 Nicosia, Cyprus

* Corresponding authors. Email address: claus@ucy.ac.cy (Claus Rebholz); Email address: allan.matthews@manchester.ac.uk (Allan Matthews), Email address: david.lewis-4@manchester.ac.uk (David J. Lewis)

Keywords: Nanoporous material, activated carbon cloth, separation, emulsions, superhydrophobicity.

Abstract

This paper reports a study involving the formation of a self-assembled polymeric monolayer on the surface of a high surface area activated carbon to engineer its affinity towards organic contaminants. A nanoporous activated carbon cloth with a surface area of ~1220 m^2/g and a pore volume of ~0.42 cm^3/g was produced by chemical impregnation, carbonisation and high-temperature CO_2 activation of a commercially available viscose rayon cloth. The subsequent modification with a silane polymer resulted in a nanoscale self-assembled monolayer that made it selective towards organic solvents (contact angle <10°) and repellant towards water (contact angle >145°). The adsorbent showed more than 95% efficiency in the separation of various types of oil/water mixtures under neutral, basic and acidic conditions. Benefiting from inherent nanoscale features, a robust hierarchical structure and a thermally stable monolayer (~300 °C), this nanoporous adsorbent maintained high efficiency for more than 20 cycles and separated surfactant stabilised emulsion with >92% oil removal efficiency. The adsorbent was studied extensively with a series of advanced characterisation techniques to establish the formation mechanism and performance in emulsion separation. Findings from this work provide crucial insights towards large-scale implementation of surface engineered activated carbon-based materials for a wide range of industrial separation applications.

Introduction

Manufacturing and energy industries have accelerated global economic growth in all areas of life for the last few decades, which have led to enhanced fossil fuel consumption and carbon emissions. As a result, industrial wastes and concomitant contamination of freshwater streams by effluents have overwhelmed the natural balance of biomes. A recent report on global warming anticipates profound changes in the human way of life by 2050 if there are no major changes implemented [1]. Therefore, environmental regulations are steering industries to green and sustainable practices whilst reducing the carbon footprint at the sources. More efficient and smart materials are sought to transition to green industrial practices and treat the already contaminated water streams. Surfactant stabilised emulsions make up a significant fraction of water contaminants and are created due to industrial operations or the extraction/refining of crude oil. Worldwide production of water associated with refining reached an average of 210 million barrels in 1999 whilst more than 4888 million barrels were released from offshore platforms in 2003 [2,3]. Unsolicited discharge of these mixtures and industrial effluents risks contaminating freshwater streams through adsorption in soil or direct mixing [4]. Finely distributed oil droplets in the water phase make an oil/water mixture more toxic and immune to conventional separation techniques. Typical oil/water separation methods lack efficiency in removing emulsion formed in the presence of natural additives and environmental stressors. Methods such as on spot burning and dispersants cause further pollution and are not sustainable for long term applications. An efficient and scalable separation method will have environmental remediation applications and enhance the economic value of industrial processes. .

Superhydrophobic materials have the potential to separate oil/water mixtures due to their selective affinity towards oil [5–13]. Several types of superhydrophobic nanocomposites,

including nanoparticle-grafted meshes, membranes, foams and textiles have been developed for this purpose [14–18]. For example, carbon-based nanofibres were grafted on a polydimethylsiloxane framework to enhance roughness, hydrophobicity and capillaries to absorb oil/water mixtures [6]. Another work reported a nanofibrous electrospun polyimide membrane containing zeolitic imidazolate framework-8@thiolated graphene [19]. The hierarchical zeolitic imidazolate framework created a superhydrophobic/superoleophilic membrane that separated oil/water mixtures and emulsions with 99% efficiency. Industrial applications of current superhydrophobic formulations are impeded by low durability and further compounded by complicated manufacturing routes [20]. Most studies used nanoparticle-based coatings that can fracture during infield application, thus changing the adsorbent properties. Adsorbents for oil/water separation must resist environmental stressors and their manufacturing route should be scalable for commercial applications.

Activated carbon (AC) is a sustainable material for adsorption of both liquid and gaseous pollutants as well as for energy storage devices due to its lightweight nature, excellent recyclability, plethora of available manufacturing processes, good commercial availability and low production costs [21,22] These features, combined with its well-developed pore structure, large pore volume and surface area, plethora of functional groups and potential for scaling up, give this material advantages over existing alternative purification materials [23,24]. AC is thermally stable, water-insoluble and resistant to organic solvents and reusable for long term commercial applications. Hence, AC has been used for applications such as the removal of both inorganic and organic pollutants, catalysis, energy storage and gas storage and separation [25–27]. Recently, AC was used for mercury removal from aqueous solution; mercury adsorption followed the pseudo-second-order model favored by some surface functionalities such as carbonyl, carboxyl and ester functional groups [28]. In another study, mesoporous AC with a

surface area of ~414 $m^2 g^{-1}$ was produced from black wattle bark waste and used to adsorb phenol from aqueous solutions [29].

High ash content, weak selectivity and universal affinity towards various pollutants make AC ineffective for treating complex organic wastes [30–32]. Similarly, surface modification of AC can improve its affinity towards organic pollutants and provide a cost-effective and scalable alternative to the current oil/water separation materials that may involve a complicated manufacturing route and are unstable to harsh operational conditions [14]. Previously, treatments with acids/bases, ozone, polymers, heat, plasma as well as nanoparticles coating have been studied to modify AC's surface for various applications [32–38]. Examples include the surface modification with ammonium persulfate for benzene adsorption [33] or grafting *N*-[(3-trimethoxysilyl)propyl]-ethylenediaminetriacetic acid to the AC surface for the removal of rare earth elements [39]. Our previous work investigated the use of nanoporous activated carbon for gas adsorption, storage and separation [40]. We propose a high surface area functionalised AC to separate oil/water mixtures and emulsions using a commercially viable cellulose-based precursor. A combination of chemical impregnation, carbonisation and high-temperature activation converted a commercial viscoce rayon cloth to a nanoporous and high surface area activated carbon cloth (ACC). Later, a self-assembled monolayer was formed on the ACC surface by a chemical reaction with 1*H*, 1*H*, 2*H*, 2*H*-Perfluorodecyltrichlorosilane (FDTS). FDTS formed a self-assembled monolayer through Si-O linkage to the surface, resulting in a functional, nanoporous and high surface area ACC (denoted hereafter as FACC). Modification of the ACC surface with FDTS serves many purposes, including grafting low surface tension of CF_3 end groups (15 dyn/cm) and enhancing nanostructures on the surface. The functionalised material was extensively characterised for its chemical and physical properties and later used to separate oil/water mixtures and emulsions. The stable surface functionality and its inherent nanostructure makes this material superior for commercial applications as

compared to traditional superhydrophobic formulations. Moreover, the process is cost-effective, straightforward and scalable. Results from this study provide fundamental knowledge for fabrication and surface modification of nanoporous materials and their potential commercial applications in removing organic contaminants.

Materials and Methods

Materials

Viscose rayon cloth was obtained from the Viskoza Factory (Loznica, Serbia). Ammonium chloride (NH_4Cl) and zinc chloride ($ZnCl_2$) were provided by Zorka. Span 80 (viscosity 1000−2000 mPa·s at 20 °C), Methylene Blue and Sudan Red dyes were procured from Sigma-Aldrich. FDTS was purchased from Fisher Scientific. Organic solvents, including toluene, hexane, acetone and methanol, were procured from Fisher Scientific. All reagents were used in as-received condition without any further processing.

ACC synthesis

The ACC synthesis steps were adapted from Babic and co-workers [41,42]. A viscose rayon cloth was used as a carbon precursor and was impregnated in a mixture of $ZnCl_2$ and NH_4Cl (both 4.0 wt%). The soaked cloth was dried at 80 °C for 40 min and later thermally treated in a vertical furnace at 630 °C under N_2 atmosphere (heating rate of 5 °C/min). After 2 h of carbonisation, the gas flow was changed to CO_2, and the furnace temperature was raised to 930 °C (heating rate of 5 °C/min). The gas flow was switched back to N_2 after 1 h of CO_2 activation and the sample was left to cool down to room temperature inside the furnace. The ACC obtained through this process was washed with distilled water and air-dried at 110 °C for 40 min before chemical functionalisation.

ACC functionalisation

A 40 mm × 40 mm piece of ACC was added in a 100 ml hexane in a beaker under continuous stirring. Later, FDTS was added (100 µL/L) and the temperature of the hotplate was raised to 100 °C until the solvent was evaporated. The sample was left to heat for another 2 h, was then collected and washed with acetone several times and finally dried in an oven at 80 °C for 1 h.

Characterisation studies

Morphological analysis and elemental mapping was carried out by field emission scanning electron microscopy (FEI-SEM Quanta 250 FEG-SEM + Gatan 3view) coupled with energy-dispersive X-ray spectroscopy (EDX, Oxford instruments). Samples were affixed on an aluminium stub with carbon tape and sputter-coated with a thin layer of platinum before microscopic analysis to improve their conductivity and avoid charging effects during imaging.

Chemical structure was analysed by Fourier-transform infrared spectroscopy (FTIR, NICOLET 5700 spectrometer) whilst X-ray photoelectron spectroscopy (XPS, Scienta Omicron XPS-Lab and Kratos Axis Ultra equipped with a monochromatic Al Kα X-ray source) was used to measure nanoscale surface composition. XPS data processing was performed with the CasaXPS software using a Shirley background for peak fitting. All spectra were rectified for C1s peak (285 eV). Carbon nature and crystal structure was studied by Raman spectroscopy and X-ray diffraction (XRD). Raman spectra were collected by a confocal spectrometer (Jobin-Yvon LABRAM) equipped with a frequency-doubled Nd-YAG laser emitting at 532.2 nm and a Peltier-cooled slow-scan charge-coupled device (CCD) matrix detector. The laser beam was focused onto the samples by a microscope (Olympus BX 40) fitted with a ×50 long-working distance objective lens at a power density of 0.1 mW/μm^2 and a spatial resolution of 1.5 cm^{-1}. Raman shifts were acquired in the wavenumber region of 500–2000 cm^{-1}. X-ray diffractograms were obtained using a Bruker AXS D8 Advance Eco diffractometer equipped with a Cu Kα X-ray tube (wavelength λ ~0.154 nm) and a LYNXEYE-XE energy-sensitive detector using 40 kV voltage and 25 mA current. The XRD measurements were performed in Bragg-Brentano geometry using a continuous scan speed mode in the diffraction angle (2θ) range of 10–60°, a step width of 0.01° and an exposure time of 1 s/step. The samples were placed onto zero-background sample holders.

Surface area and pore structure was investigated by recording low-pressure (0–1 bar) CO_2 adsorption isotherms at 0 ^oC by a manometric gas sorption analyser (Quantachrome Autosorb iQ3) coupled with an external temperature controlling device and a circulating bath filled with a mixture of water and anti-freezing liquid. Ultra-pure (99.999%) He and CO_2 gases were used for void volume calculations and gas sorption analysis, respectively. All samples (~30 mg) were degassed under high vacuum (10^{-6} mbar) at 200 ^oC for 24 h before analysis to remove any physisorbed surface species. The specific surface area (SSA), specific pore volume (SPV) and pore size distribution (PSD) values of the degassed samples were calculated by applying the CO_2-carbon Grand Canonical Monte Carlo (GCMC) equilibrium transition kernel at 0 ^oC based on slit pores in the measured CO_2 adsorption data [43].

Thermal gravimetric analysis (TGA, Seiko SSC/S200 instrument) was used to study the thermal stability and degradation of chemical groups in the 30-1000 ^oC temperature range under N_2 atmosphere using a heating rate of 10 °C/min. Hydrophobicity of the FACC sample was analysed by measuring the static water drop contact angle (Kruss FTA 100 drop shape analyser). The samples were cut in small pieces (20 mm × 20 mm) and placed on the sample stage of the drop shape analyser.

Oil/water separation efficiencies were determined only for the FACC sample by using a 1:1 oil/water mixture. Both water and oil were dyed with methylene blue and Sudan red dye, respectively. The FACC material was placed in the filtration system, before the oil/water mixture was poured through the FACC and the efficiency was calculated by observing the volumes of both liquids. The efficiencies were adjusted by adding the volume of liquid adsorbed by the cloth. Emulsion separation was performed by converting the FACC sample into powder using mortar and pestle. The powder was washed and then dried in an oven at 20 ^oC for 24 h. Emulsions were prepared by mixing toluene and a surfactant (Span 80, 1g/L) in

water with a magnetic stirrer. A known quantity of emulsion was taken in a glass vial and mixed with different amounts of FACC powder using a vortex mixer. Emulsion separation efficiency was observed by analysing the total organic carbon content (TOC-Shimadzu, TOC-V CPN) in emulsion before and after treatment. Further, the presence of toluene was detected by recording the absorbance spectra in samples before and after separation using ultraviolet visible (UV-vis) spectroscopy. The samples were diluted 10 times with deionised water before TOC and UV-vis analysis.

Results and Discussion

A Scanning Electron Microscope (SEM) was used for the morphological analysis and elemental mapping of both ACC and FACC samples. Figure 1 shows the SEM images of both samples at different magnifications accompanied by elemental maps. Both samples have a hierarchical morphology that spans from woven yarns (250-300 µm in width) to individual carbon fibres a few micrometers in diameter. Microscopic fibres (10-20 µm in width) are entwined to form a macroscopic fabric. High magnification images reveal the pleated texture (~1 µm) of individual fibres that adds to the overall roughness of the material. The EDS map of the ACC sample shows three elements (see Figure 1a; right side). O and C form the bulk structure of the carbonaceous material, whilst Pt originates from the thin conductive coating applied before SEM analysis. A significant amount of the O signal can be from adsorbed moisture and oxygenated functional groups. Figure 1b shows the SEM and EDS maps of the FACC sample. The structural integrity and hierarchical roughness of the pristine ACC surface is maintained post-functionalisation. Two new elements (i.e. F and Si) are observed in the EDS maps that indicate grafting of functional groups on the surface. The uniformity of the F and Si elemental maps confirms the consistent surface chemistry throughout the functionalised fabric.

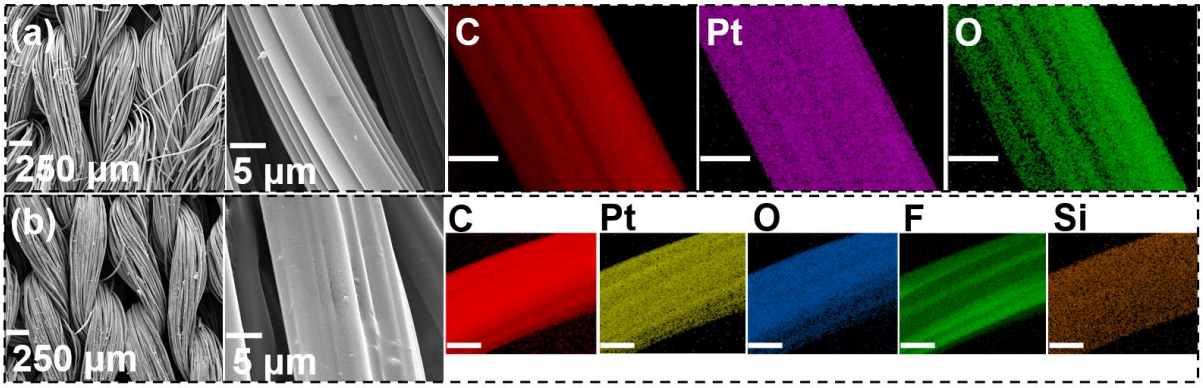

Figure 1: SEM images and EDS mapping of (a) pristine ACC (b) FACC materials. Si and F appear in the EDS map of FACC, thus confirming the functionalisation of the ACC surface. The uniform distribution of these elements ensures an even surface chemistry throughout the fibre surface.

FTIR provided more information about the chemical structure of the fabric before and after functionalisation. The spectra in Figure 2 show the types of bonds present in both samples. Pristine ACC shows a broad band from 3700 cm^{-1} to 2800 cm^{-1}, which corresponds to the stretching vibrations of hydroxyl groups (O-H), along with a weaker band around 1550 cm^{-1}, which is most probably related to the stretching vibration of sp^2 carbon and/or the presence of oxygen-based surface functionalities (e.g. carbonyls and carboxyls) [40]. Instead, the FACC sample showed a quite different bond structure. The two sharp peaks at 1200 cm^{-1} and 1139 cm^{-1} and the other smaller peaks in the range 1100 cm^{-1} to 1270 cm^{-1} are associated with vibrations of CF_2 and CF_3 functional groups and C-C and C-F pairing [44–46]. A small peak at 1090-1040 cm^{-1} can be assigned to the stretching vibration of Si-O-Si bond [47,48]. Another key feature is the receding of the characteristic band across 3000 cm^{-1} post-functionalisation. This is due to the formation of a self-assembled monolayer that replaced the hydroxyl groups and, therefore, hampered the fabric's ability to adsorb moisture/water.

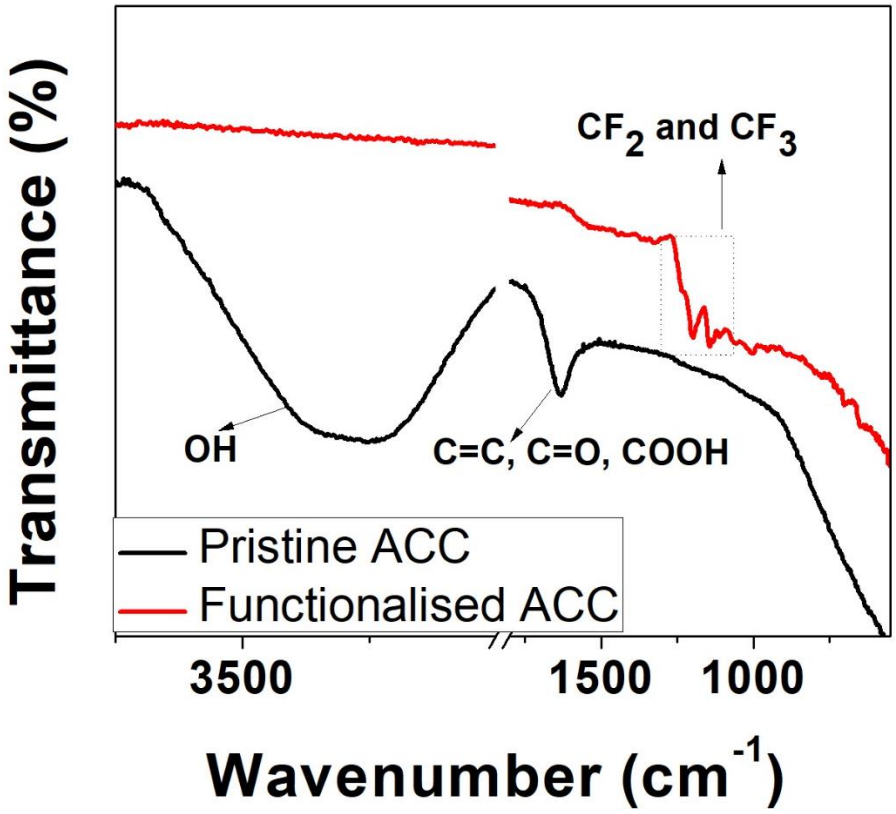

Figure 2: FTIR spectra of pristine ACC and FACC materials showing the differences in functional groups before and after treatment with silane. The intensity of hydrophilic groups is reduced post-functionalisation, and the two new peaks corresponding to CF_2 and CF_3 groups confirm the grafting of silane.

XPS provided information about the nanoscale surface chemical composition and chemical state [49,50], which is imperative to study the formation mechanism of self-assembled monolayers on the ACC surface. The XPS survey spectra of the ACC sample and the high-resolution C1s peak are shown in Figures 3a and 3b, respectively. The pristine ACC contains 83 at.% carbon and 12 at.% oxygen as primary elements, with a C/O ratio of 6. Other elements include N, Zn, Cl and Si in at.% of 2., 0.22, 0.57 and 0.99, respectively, which originate from the impregnation and carbonisation stages of the ACC synthesis procedure. Previous reports have suggested similar C/O ratios for a mesoporous activated carbon prepared by different precursors. For example, porous carbons prepared from food waste contained 81.9 at.% C and 13.6 at.% oxygen [51]. Deconvolution of high-resolution C1s spectra shows the chemical state of carbon in

the ACC sample. The prominent peak at 285 eV indicates C=C bond whilst other components are assigned to C-O, C=O, and O-C=O bonds [40]. XPS spectra of the FACC sample show two additional F and Si peaks that emerge from the surface groups (see Figure 3c). The chemical composition of the FACC sample indicates a decrease of both C and O contents to 35.9 at.% and 7.4 at.%, respectively, whilst F is a significant element with 53.4 at.% and Si as 3.4 at.%. This is because XPS analysis only probes the surface of the sample (~6-10 nm in depth) and most of the elemental composition arises from the fluorosilane surface functional groups. This is further confirmed by the deconvolution of the C1s peak (see Figure 3d), which shows an entirely different carbon state compared to the C1s spectra of the pristine ACC sample. Peaks around 291 eV and 293 eV are assigned to CF_2, and CF_3 groups, respectively, whilst the peak around 285 eV is attributed to C-C and C-H chemical states of carbon [52,53]. The XPS analysis verified the findings from FTIR and EDX spectroscopy.

.

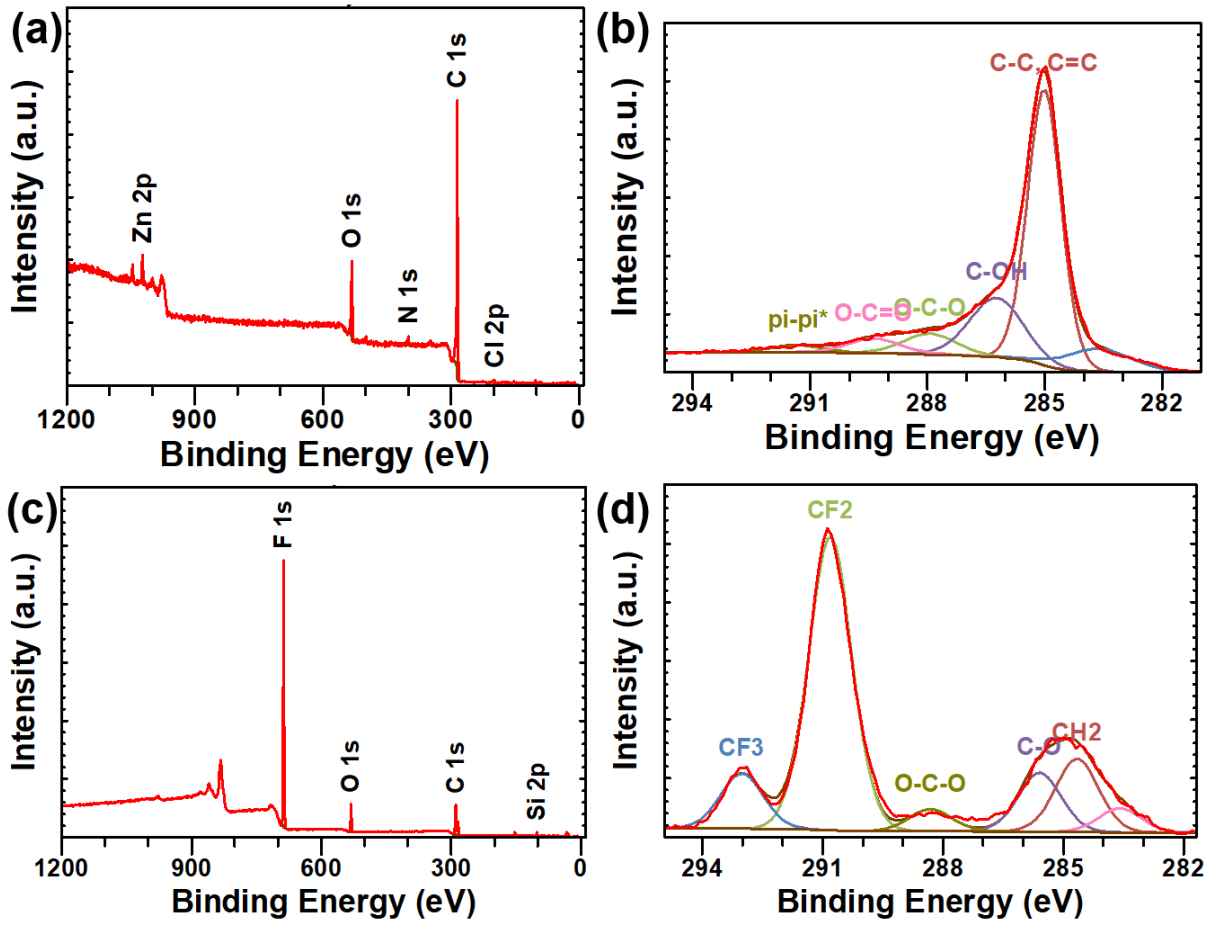

Figure 3: Survey and high-resolution XPS emission spectra of pristine ACC and FCC materials; (a) ACC survey spectrum, (b) high-resolution C1s spectrum of ACC, (c) FACC survey spectrum and (d) high-resolution C1s spectrum of FACC.

Raman spectra (Figure 4a) indicate the carbonaceous structure of both samples. Two characteristic peaks can be observed in the wavenumber range 500-2000 cm^{-1}: the defect-induced D band at ~1344 cm^{-1}, from the breathing vibration of sp^3 hybridised carbons, and the graphitic G band at ~1609 cm^{-1}, associated with the stretching vibration of sp^2 hybridised carbons in the hexagonal lattice [54]. The disorder in the structure is reflected by the high intensity ratios of the D/G bands (i.e. I_D/I_G ~0.99) [55,56]. Powder X-ray diffraction patterns of both samples show two broad peaks centred at 2θ ~23° and ~44° that correspond to the (002) and (100) carbon reflections, respectively. The (002) peak is shifted considerably to lower 2θ values in comparison to crystalline graphite (i.e. located at 26.5°), thus indicating a larger interlayer

spacing (i.e. more than 0.334 nm; see JCPDS card no. 75-1621). Both samples showed a graphitic structure, resembling randomly orientated stacked graphene sheets [57]. XRD patterns of both samples (Figure 4b) suggest a turbostratic disorder with considerable distortion in the stacking of their graphene layers [58]. The Raman spectra and X-ray diffractograms lead to the same conclusion that the surface modification did not affect the crystallinity of the material. Despite the difference in peak intensity, FACC did not show any crystal structure variation after the assembly of the fluorosilane layer. It has been observed in a previous study that a fluorosilane coating on a graphene sheet did not alter crystalline quality [59].

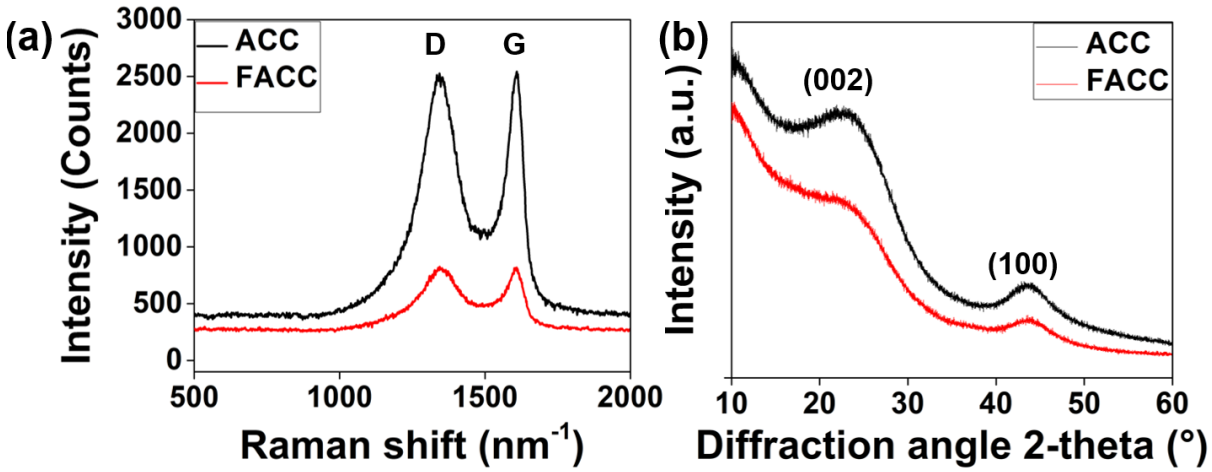

Figure 4: (a) Raman spectra of both ACC and FACC materials with characteristic D and G bands at 1344 cm^{-1} and 1609 cm^{-1}, respectively, and (b) X-ray diffractograms with two peaks around 23° and 44° corresponding to (002) and (100) reflections of turbostratic carbon, respectively.

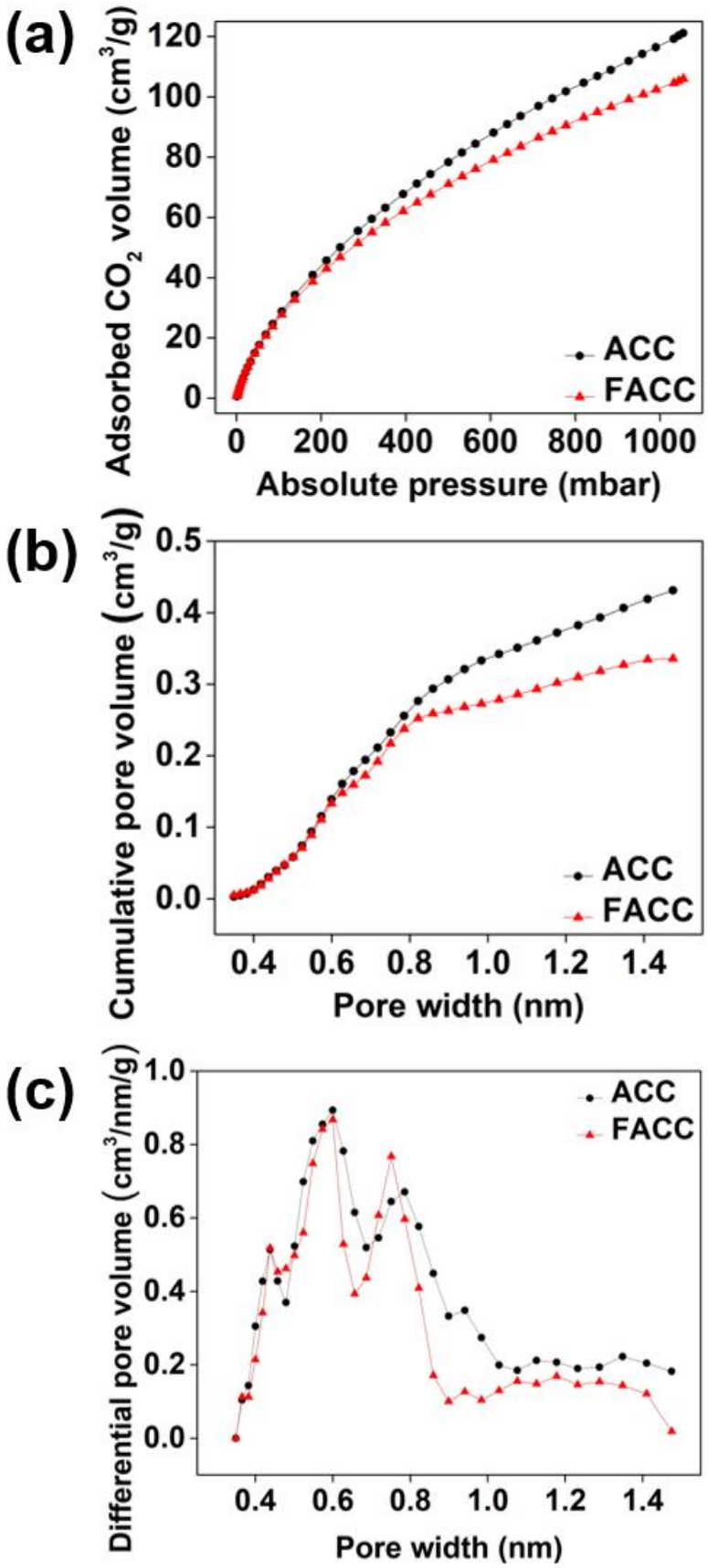
(a)
Adsorbed CO_2 volume (cm^3/g)
120
100
80
60
40
20
0
0
200
400
600
800
1000
Absolute pressure (mbar)
ACC
FACC
(b)
Cumulative pore volume (cm^3/g)
0.5
0.4
0.3
0.2
0.1
0.0
0.4
0.6
0.8
1.0
1.2
1.4
Pore width (nm)
ACC
FACC
(c)
Differential pore volume (cm^3/nm/g)
1.0
0.8
0.6
0.4
0.2
0.0
0.4
0.6
0.8
1.0
1.2
1.4
Pore width (nm)
ACC
FACC

Figure 5: (a) CO_2 adsorption isotherms recorded at 0 ^oC for the degassed ACC and FACC materials, (b) cumulative and (c) differential pore size distribution analysis using the GCMC method for slit pores in the recorded CO_2 adsorption data.

Low-pressure (0-1 bar) CO_2 adsorption isotherms at 0 ^oC are presented in Figure 5a. The adsorbed CO_2 volume at ~1 bar reduced by ~13% upon functionalisation of the ACC surface; i.e. ~121 and ~106 cm^3/g for the ACC and FACC samples, respectively. In a similar manner, the cumulative surface area, as derived by applying the GCMC kernel for slit pores, showed a ~16% drop upon surface modification; i.e. ~1217 and ~1019 m^2/g for the ACC and FACC samples, respectively. The cumulative pore size distribution (PSD) graphs, based on the GCMC method, are presented in Figure 5b. The cumulative pore volume for pore widths below 1.5 nm showed a reduction of ~21% upon surface modification; i.e. ~0.43 and ~0.34 cm^3/g for the ACC and FACC samples, respectively. The differential PSD graphs (Figure 5c) of both samples show three distinct peak maxima at ~0.45, ~0.60 and ~0.75 nm, pointing to dominant ultra-microporosity (i.e. pore widths below 0.7 nm). Hence, the gas sorption data suggest that even though there is small reduction in the cumulative surface area and pore volume values of the FACC material, the ultra-microporous structure seems to be maintained upon surface functionalisation.

Fabrication of AC involves carbonisation of a precursor towards transformation to carbon and then a subsequent activation step to tune the surface area, pore volume and pore size. The properties of AC depend on the precursor material and its processing conditions. For cellulosic materials, carbonisation starts from physical desorption of water up to ~150 ^oC, followed by dehydration of the cellulose unit up to ~240 °C. Further rise in temperature leads to cleavage

of the glycosidic bond and splitting of the C-C and C-O bonds up to 400 °C and as a final step aromatisation above 400 °C [60,61]. Prior to the carbonisation, an impregnation step in a mixture of NH_4Cl and $ZnCl_2$ catalysts was exploited to reduce the pyrolysis time and increase the carbon yield by promoting dehydration over depolymerisation [40]. CO_2 penetrated and etched the carbon sheets in the high-temperature oxidation step, thus facilitating pore formation and development of a high surface area [62,63]. The resulting high surface area and nanoporous ACC could have abundant oxygen functionalities that can act as seeding sites for a self-assembled monolayer . It is concluded from the EDS, FTIR and XPS results that FDTS reacted with the surface groups and formed a Si-O linkage with the ACC surface. The reaction involved hydrolysis and condensation at the ACC surface. Hydrolysis generated $–Si(OH)_3$ moieties which later condensed to form a –(Si-O-Si)– network. The presence of CF_2 and CF_3 bonds in the FTIR spectra, together with the uniformity shown in the EDS maps and the chemical composition by XPS confirms the grafting of a uniform monolayer which substituted surface hydroxyl groups, thus conferring a low surface energy to the fabric. A combination of high surface area, nanoporous structure and low surface energy could lead to a highly hydrophobic functional adsorbent that can be used to adsorb oil from oil/water mixtures and emulsions.

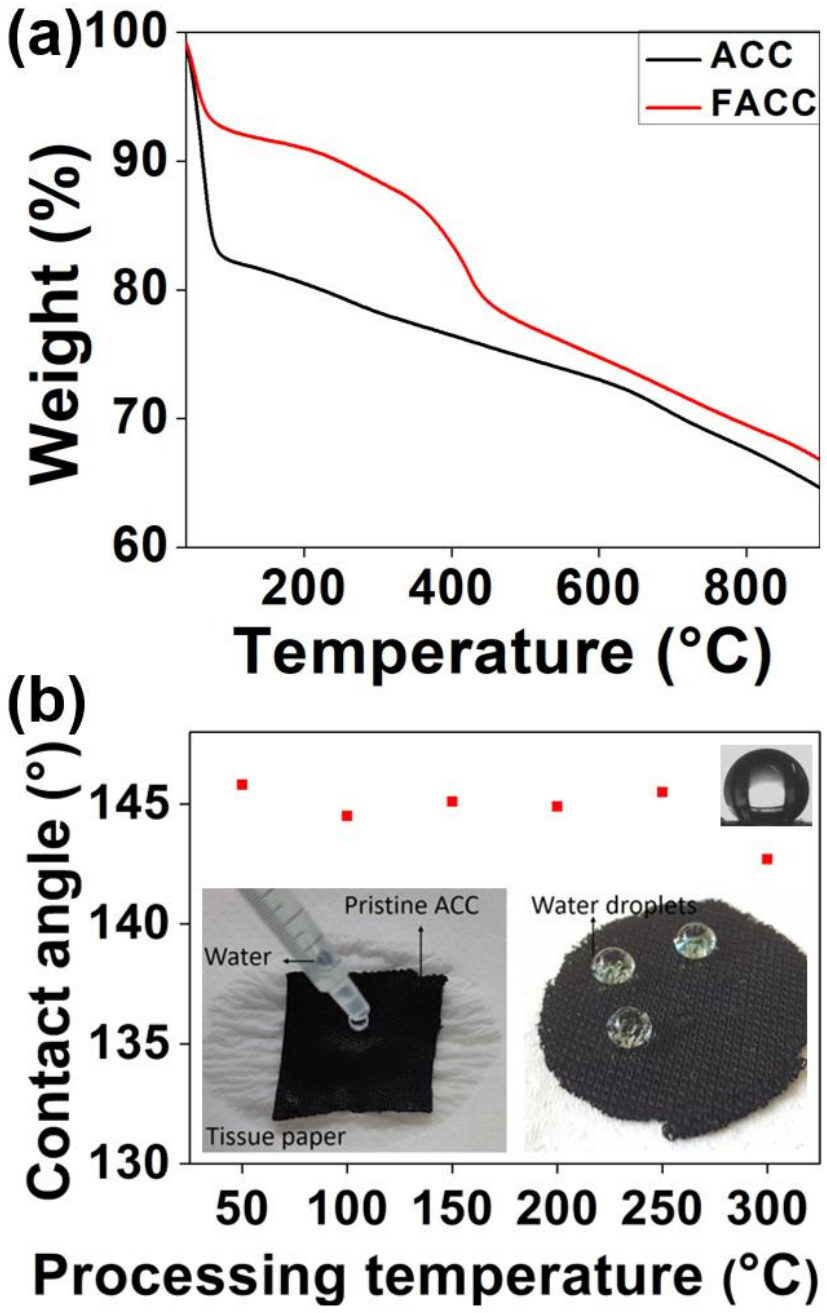

Figure 6: (a) TGA profiles of the ACC and FACC materials under a N_2 atmosphere and (b) contact angle measurements of the FACC sample processed at different temperatures; the inset shows that the pristine ACC readily absorbs water whilst the FACC is repellant towards water and causes the droplets to form as spherical beads with contact angles higher than 145^o demonstrating hydrophobicity.

The TGA analysis provided information about the thermal stability of surface functional groups. Figure 6 shows the TGA profile of both ACC and FACC samples. The first weight loss (~18 %) in ACC between ~40-100 °C corresponds to the removal of adsorbed moisture. This

is followed by a continuous weight loss due to degradation of surface groups and retained organic compounds. Weight loss in activated carbons in this region has been previously attributed to retained cellulose, oxygen containing surface groups, volatile organic compounds [64,65]. FACC shows a minimal weight loss due to moisture (~8%) owing to its hydrophobic nature. A significant weight loss due to removal of fluorosilane functionalities in the FACC sample (~10%) starts at ~330 °C and goes up to ~470 °C. Considering the stability of functional groups, FACC can maintain its hydrophobic functionalities up to 330 °C. Contact angle measurements further evaluated hydrophobicity at room temperature and for samples processed at different temperatures. ACC demonstrated a superhydrophilic behaviour, as shown in the inset of Figure 6b (left), where water droplets were readily absorbed by the fabric. Instead, water droplets formed spherical beads when they came into contact with the FACC surface, as shown in the inset of Figure 6b (right), thus highlighting a hydrophobic behaviour.

The samples were treated in a furnace for 1 h at 50, 100, 150, 200, 250 and 300 °C and then washed and dried for contact angle measurements. The FACC sample maintained a water contact angle (WCA) of ~145° in all cases except at 300 °C, where a slightly smaller contact angle was observed probably due to degradation of some of the functional groups.

Despite repellence towards water, organic solvents and oils readily fill the porous structure upon interaction with the FACC surface. Figure 7a shows the selective adsorption of toluene (red coloured) from the water (blue coloured) solution using the FACC sample. Toluene interacted with the non-polar surface functional groups and was able to immerse into the fabric due to low surface tension, whilst the water could not interact due to the extremely hydrophobic nature. Selective affinity towards organic solvents enables the FACC material to capture oil from oil/water mixtures and emulsion. Owing to the combination of hydrophobic and superoleophilic properties, FACC was used to separate oil/water mixtures through a gravity-

driven filtration system, as shown in Figure 7b. A typical 1:1 toluene/water mixture was used to demonstrate the separation process and efficiency was measured by calculating the volumes for both liquids before and after separation. The mixture was poured through the filtration system, oil passed through the FACC material and was collected in a funnel at the bottom of the filtration system whilst water was blocked due to the FACC's hydrophobic properties, as shown in Fig 7b. Oil/water separation efficiency was maintained up to ~98% for more than 20 cycles. More than 95 % separation efficiency was observed for different types of oils, including hexane, toluene, heptane and dichloromethane, as shown in Figure 7c. A gravity based filtration system using a FACC sample as separation membrane presents an excellent solution for separating oil/water mixtures, where oil can be quickly drained through and water is collected from the top.

Most superhydrophobic materials cannot perform well in corrosive environments and high temperatures (> 50 °C) due to unstable surface groups, mechanical wear due to water impact, or low surface tension at high temperatures [66]. In-field application of oil/water separation systems involves corrosive media and hot climates and for this reason a filtration system must maintain its functional properties in various conditions. The FACC sample was used to test oil/water separation under basic and acidic conditions, and it maintained a high separation efficiency in corrosive liquids (NaCl, NaOH and HCl) and hot water (~ 60 °C), as shown in Figure 7e. This behaviour could be attributed to two characteristics of the FACC material: 1) inherent nanoscale features without the coating of external nanoparticles and 2) strong chemical bonding between fabric and surface functional groups, as explained above.

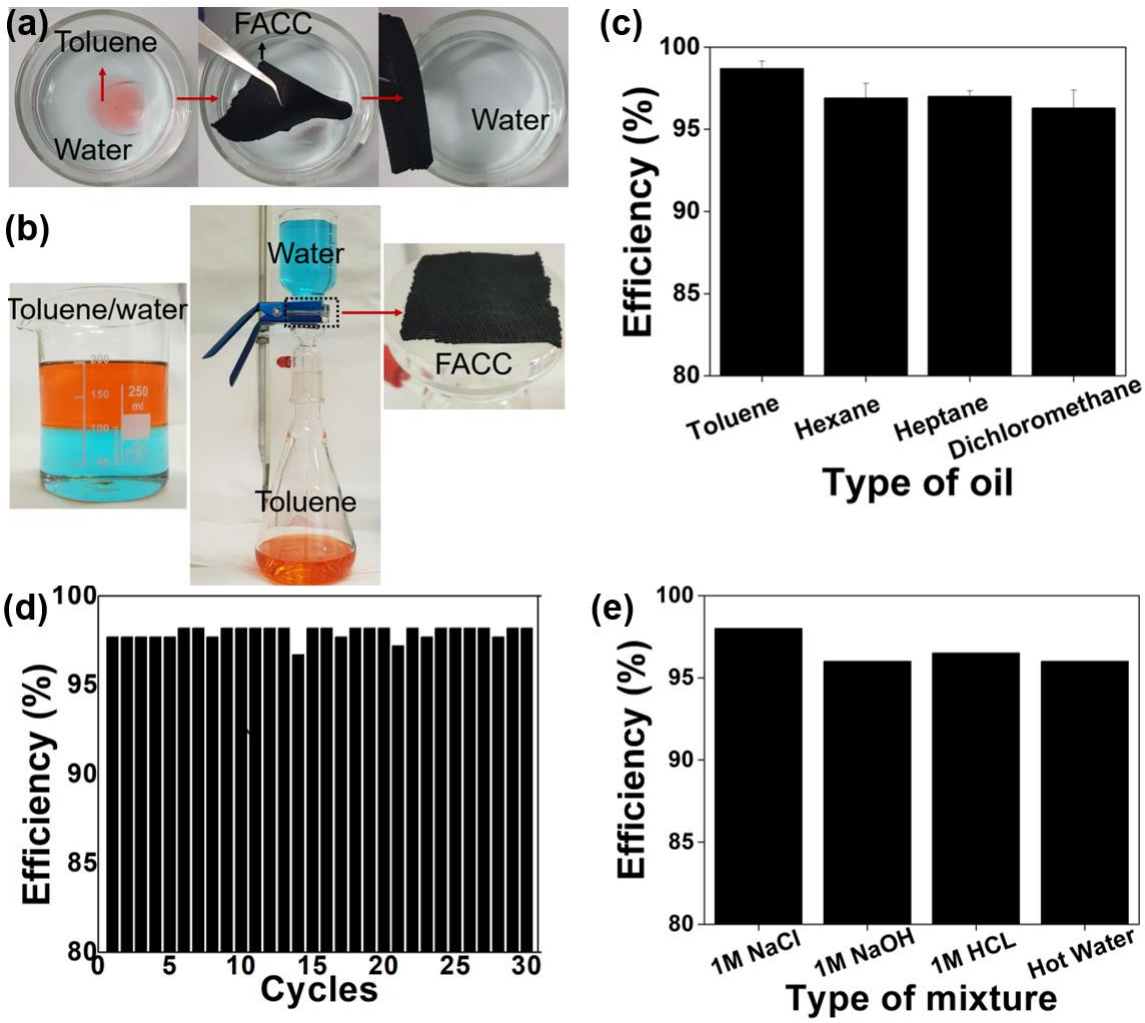

Figure 7: (a) Series of images showing the selective adsorption of toluene (dyed by Sudan red) from an aqueous solution using the FACC material; (b) series of images showing a typical oil/water mixture, separation setup used for oil/water separation, and an FACC sample used as membrane to block the passage of water (c) graph shows the oil/water efficiency of various types of oil/water mixtures, > 95% in all cases; (d) separation efficiency up to 30 cycles and (e) oil/water separation efficiency of the FACC sample in acidic and basic mixtures.

Oil/water mixtures tend to form emulsions in the presence of external stressors (high flow rate, pipeline pressure and solid residue) and natural surfactants. Tiny oil droplets uniformly dispersed in the water phase make emulsion more damaging to the environment and difficult to separate with typical filtration systems. Ceramic-, cellulose- and graphene-based superhydrophobic microfiltration membranes have been used to sieve micrometer sized oil droplets [14,67]. Here, the FACC sample was used for batch scale separation of surfactant

stabilised emulsions. Toluene-based emulsion was mixed with a known amount of FACC powder, as shown in Figure 8a, using a vortex mixer. Under optimum conditions, the FACC powder was able to adsorb uniformly distributed oil droplets from the emulsion. Figure 8b shows the emulsion images before (left) and after (right) treatment with the FACC sample. The emulsion appears cloudy before treatment due to well-dispersed oil droplets in water whilst a transparent liquid is obtained after treatment. The removal of oil from emulsion was quantified by using total organic carbon analysis.

Figure 8c shows the oil removal efficiency of the FACC powder with increasing weight. The oil concentration in the emulsion decreases significantly by adding just 50 mg of FACC powder into the emulsion and a ~62% oil removal efficiency is obtained. The separation efficiency gradually increases with increasing the FACC weight and finally reaches a plateau after 200 mg. The maximum oil removal efficiency of ~92% was obtained when the emulsion was treated with 400 mg of FACC powder. The separation efficiency was further confirmed by analysing selected samples by UV-vis spectroscopy. Figure 8d shows the absorbance spectra of the emulsion and samples treated with 50, 200 and 400 g of FACC powder. The emulsion shows very strong absorbance in the range of 225-275 nm, indicating the presence of toluene in the solution. The intensity of this peak gradually decreases with increasing the FACC weight. UV-vis results further validate TOC analysis that best oil removal efficiency is achieved with 400 g of FACC powder in this case.

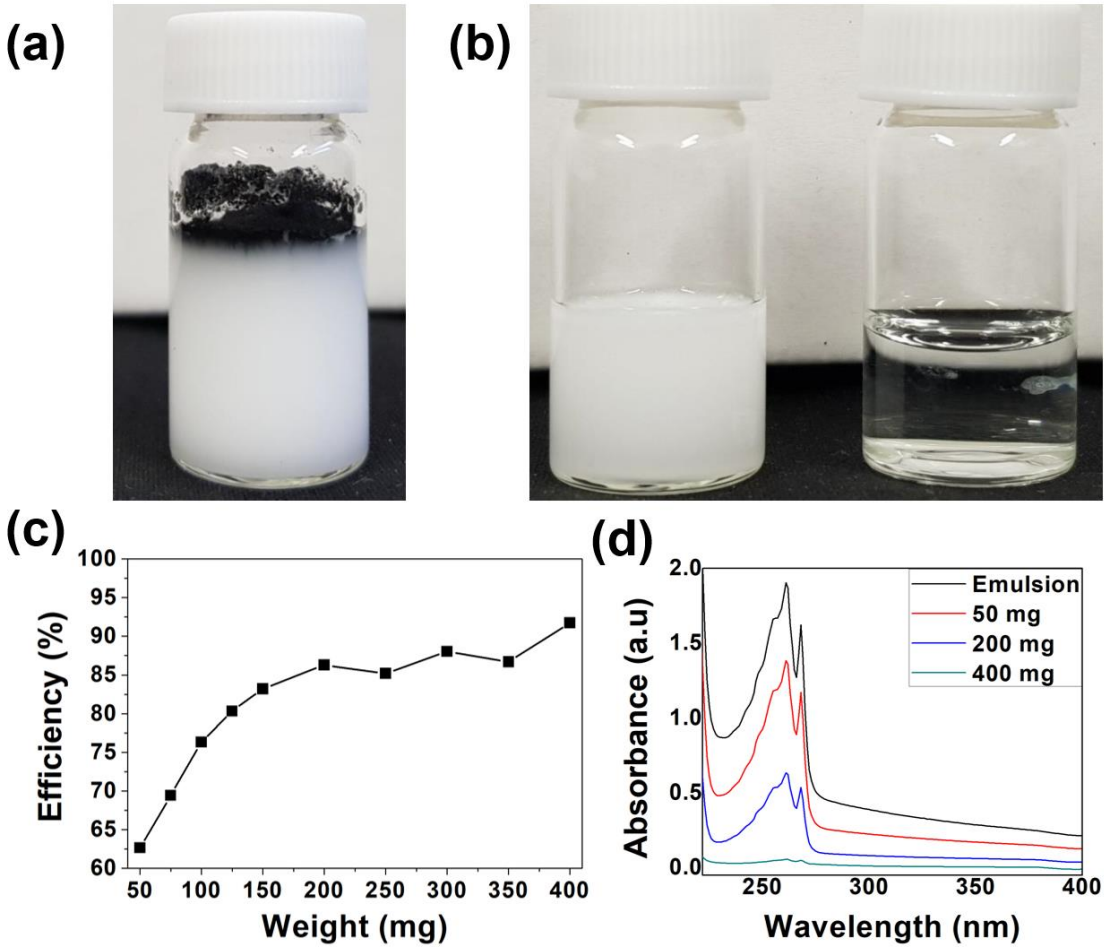

Figure 8: Series of images and data showing the emulsion separation efficiency of the FACC material; surfactant stabilised emulsion (a) before separation and (b) after separation, (c) oil removal efficiency with an increasing amount of FACC powder and (d) absorbance spectra of emulsion samples treated with different amounts of FACC powder.

In summary, the FACC material effectively separated the surfactant stabilised emulsions that cannot be separated otherwise by traditional separation methods. The unique combination of a nanoporous structure with low surface energy layer made the FACC material selective towards well-dispersed oil droplets. Hydrophobic functional groups facilitated the interaction with oil droplets and subsequent adsorption upon mixing the FACC powder with the emulsion. Furthermore, the hydrophobic adsorbent expedites tiny oil droplets' coalescence, leading to

large droplets or oil layers through collision and fusion, thus improving the overall separation efficiency [67].

We envisage this material to be combined with closed filtration systems for efficient separation of oil/water mixtures and emulsions. Although the modification layers appear to be quite robust, as evidenced by several characterisation techniques, filtration material should not be exposed or used without design considerations to prevent the potential effects of Fluorine containing compounds on the environment.

Conclusions

Nanoporous and high surface area activated carbons are promising materials for water purification applications. However, universal affinity towards contaminants restricts its application for complex oil/water mixtures. This work reported the development of pristine (ACC) and surface-modified (FACC) nanoporous and high surface area activated carbon cloths via catalyst impregnation, carbonisation under N_2 and high-temperature CO_2 activation of a commercially available cellulose-based precursor (viscose rayon cloth), followed by chemical functionalisation with FDTS. The oxygen-rich functionalities of the pristine ACC surface act as a platform for anchoring a self-assembled polymeric monolayer that showed a combined hydrophobic and oleophilic character. Robust bonding between the oxygen functional groups and the fluorosilane monolayer resulted in a thermally stable adsorbent for selective separation of oil/water mixtures. A unique combination of nanoporous structure and low surface energy functionalities enabled the FACC material to separate oil/water mixtures with high efficiency (>95%) for various cycles under various conditions. In addition, the FACC material showed an outstanding performance in the separation of surfactant stabilised emulsions with more than 92% efficiency.

Conflict of Interest

There are no conflicts of interest to declare.

Acknowledgements

N.K. would like to thank Prof. Christian Mitterer, Prof. Oskar Paris and Prof. Ronald Bakker from the Montanuniversität Leoben for providing resources and access to experimental equipment. The authors would like to thank Dr. Biljana Babic and Dr. Ana Kalijadis from the University of Belgrade for providing the ACC material.

References

(1) Spratt, D.; Dunlop, I. Existential Climate-Related Security Risk: A Scenario Approach. 2019.

(2) Khatib, Z.; Verbeek, P. Water to Value - Produced Water Management for Sustainable Field Development of Mature and Green Fields. In *International Conference on Health, Safety and Environment in Oil and Gas Exploration and Production*; Society of Petroleum Engineers (SPE), 2002; pp 91–94. https://doi.org/10.2118/73853-ms.

(3) Neff, J.; Lee, K.; DeBlois, E. M. Produced Water: Overview of Composition, Fates, and Effects. In *Produced Water*; Springer New York, 2011; pp 3–54. https://doi.org/10.1007/978-1-4614-0046-2_1.

(4) Veil, J. A.; Puder, M. G.; Elcock, D.; Redweik, R. J., Jr. *A White Paper Describing Produced Water from Production of Crude Oil, Natural Gas, and Coal Bed Methane.*; Argonne, IL (United States), 2004. https://doi.org/10.2172/821666.

(5) Kang, L.; Wang, B.; Zeng, J.; Cheng, Z.; Li, J.; Xu, J.; Gao, W.; Chen, K. Degradable Dual Superlyophobic Lignocellulosic Fibers for High-Efficiency Oil/Water Separation. *Green Chem.* **2020**, *22* (2), 504–512. https://doi.org/10.1039/c9gc03861b.

(6) Guo, Z.; Long, B.; Gao, S.; Luo, J.; Wang, L.; Huang, X.; Wang, D.; Xue, H.; Gao, J. Carbon Nanofiber Based Superhydrophobic Foam Composite for High Performance Oil/Water Separation. *J. Hazard. Mater.* **2021**, *402*, 123838. https://doi.org/10.1016/j.jhazmat.2020.123838.

(7) Yan, S.; Li, Y.; Xie, F.; Wu, J.; Jia, X.; Yang, J.; Song, H.; Zhang, Z. Environmentally Safe and Porous MS@TiO2@PPy Monoliths with Superior Visible-Light Photocatalytic Properties for Rapid Oil-Water Separation and Water Purification. *ACS Sustain. Chem. Eng.* **2020**, *8* (13), 5347–5359. https://doi.org/10.1021/acssuschemeng.0c00360.

(8) Wang, M.; Wang, M.; Zhang, Z.; Zhang, Z.; Wang, Y.; Zhao, X.; Men, X.; Yang, M. Ultrafast Fabrication of Metal-Organic Framework-Functionalized Superwetting Membrane for Multichannel Oil/Water Separation and Floating Oil Collection. *ACS Appl. Mater. Interfaces* **2020**, *12* (22), 25512–25520. https://doi.org/10.1021/acsami.0c08731.

(9) Liu, H.; Chen, X.; Zheng, Y.; Zhang, D.; Zhao, Y.; Wang, C.; Pan, C.; Liu, C.; Shen, C. Lightweight, Superelastic, and Hydrophobic Polyimide Nanofiber /MXene Composite Aerogel for Wearable Piezoresistive Sensor and Oil/Water Separation Applications. *Adv. Funct. Mater.* **2021**, 2008006. https://doi.org/10.1002/adfm.202008006.

(10) Murtaza, G.; Zulfiqar, U.; Spencer, B. F.; Venkateswaran, S. P.; Alam, F.; Lewis, D. J. Optimization of Superhydrophobicity at the Surface of Iron Sulfide Thin Films by a Wet Chemical Approach. *Mater. Res. Bull.* **2021**, *144*, 111476. https://doi.org/10.1016/J.MATERRESBULL.2021.111476.

(11) Zulfiqar, U.; Hussain, S. Z.; Subhani, T.; Hussain, I.; Habib-ur-Rehman. Mechanically Robust Superhydrophobic Coating from Sawdust Particles and Carbon Soot for

Oil/Water Separation. *Colloids Surfaces A Physicochem. Eng. Asp.* **2018**, *539*. https://doi.org/10.1016/j.colsurfa.2017.12.047.

(12) Zulfiqar, U.; Hussain, S. Z.; Awais, M.; Khan, M. M. J.; Hussain, I.; Husain, S. W.; Subhani, T. In-Situ Synthesis of Bi-Modal Hydrophobic Silica Nanoparticles for Oil-Water Separation. *Colloids Surfaces A Physicochem. Eng. Asp.* **2016**, *508*. https://doi.org/10.1016/j.colsurfa.2016.08.074.

(13) Bano, S.; Zulfiqar, U.; Zaheer, U.; Awais, M.; Ahmad, I.; Subhani, T. Durable and Recyclable Superhydrophobic Fabric and Mesh for Oil-Water Separation. *Adv. Eng. Mater.* **2017**. https://doi.org/10.1002/adem.201700460.

(14) Zulfiqar, U.; Thomas, A. G.; Matthews, A.; Lewis, D. J. Surface Engineering of Ceramic Nanomaterials for Separation of Oil/Water Mixtures. *Frontiers in Chemistry*. Frontiers Media S.A. November 19, 2020, p 578. https://doi.org/10.3389/fchem.2020.00578.

(15) Latthe, S. S.; Kodag, V. S.; Sutar, R. S.; Bhosale, A. K.; Nagappan, S.; Ha, C. S.; Sadasivuni, K. K.; Kulal, S. R.; Liu, S.; Xing, R. Sawdust-Based Superhydrophobic Pellets for Efficient Oil-Water Separation. *Mater. Chem. Phys.* **2020**, *243*, 122634. https://doi.org/10.1016/j.matchemphys.2020.122634.

(16) Zulfiqar, U.; Thomas, A. G.; Yearsley, K.; Bolton, L. W.; Matthews, A.; Lewis, D. J. Renewable Adsorbent for the Separation of Surfactant-Stabilized Oil in Water Emulsions Based on Nanostructured Sawdust. *ACS Sustain. Chem. Eng.* **2019**, acssuschemeng.9b04294. https://doi.org/10.1021/acssuschemeng.9b04294.

(17) Zhu, L.; Li, H.; Yin, Y.; Cui, Z.; Ma, C.; Li, X.; Xue, Q. One-Step Synthesis of a Robust and Anti-Oil-Fouling Biomimetic Cactus-like Hierarchical Architecture for Highly Efficient Oil/Water Separation. *Environ. Sci. Nano* **2020**, *7* (3), 903–911. https://doi.org/10.1039/c9en01140d.

(18) Zhang, M.; Wu, Z.; Meng, F.; Lin, H. Facile Preparation of Grass-like Hierarchical Structured γ-AlOOH Coated Stainless Steel Mesh with Superhydrophobic and Superoleophilic for Highly Efficient Oil-Water Separation. *Sep. Purif. Technol.* **2019**, *212*, 347–354. https://doi.org/10.1016/J.SEPPUR.2018.08.069.

(19) Ma, W.; Li, Y.; Zhang, M.; Gao, S.; Cui, J.; Huang, C.; Fu, G. Biomimetic Durable Multifunctional Self-Cleaning Nanofibrous Membrane with Outstanding Oil/Water Separation, Photodegradation of Organic Contaminants, and Antibacterial Performances. *ACS Appl. Mater. Interfaces* **2020**, *12* (31), 34999–35010. https://doi.org/10.1021/acsami.0c09059.

(20) Zulfiqar, U.; Thomas, A. G.; Matthews, A.; Lewis, D. J. Surface Engineering of Ceramic Nanomaterials for Separation of Oil/Water Mixtures. *Frontiers in Chemistry*. Frontiers Media S.A. November 19, 2020, p 578. https://doi.org/10.3389/fchem.2020.00578.

(21) Zheng, W.; Chen, S.; Liu, H.; Ma, Y.; Xu, W. Study of the Modification Mechanism of Heavy Metal Ions Adsorbed by Biomass-Activated Carbon Doped with a Solid Nitrogen Source. *RSC Adv.* **2019**, *9* (64), 37440–37449. https://doi.org/10.1039/c9ra07191a.

(22) Liu, W. J.; Jiang, H.; Yu, H. Q. Emerging Applications of Biochar-Based Materials for

Energy Storage and Conversion. *Energy and Environmental Science*. Royal Society of Chemistry June 1, 2019, pp 1751–1779. https://doi.org/10.1039/c9ee00206e.

(23) Wang, H.; Xu, J.; Liu, X.; Sheng, L. Preparation of Straw Activated Carbon and Its Application in Wastewater Treatment: A Review. *Journal of Cleaner Production*. Elsevier Ltd February 10, 2021, p 124671. https://doi.org/10.1016/j.jclepro.2020.124671.

(24) Santoso, E.; Ediati, R.; Kusumawati, Y.; Bahruji, H.; Sulistiono, D. O.; Prasetyoko, D. Review on Recent Advances of Carbon Based Adsorbent for Methylene Blue Removal from Waste Water. *Materials Today Chemistry*. Elsevier Ltd June 1, 2020, p 100233. https://doi.org/10.1016/j.mtchem.2019.100233.

(25) Zhang, M.; Cheng, J.; Zhang, L.; Li, Y.; Chen, M. S.; Chen, Y.; Shen, Z. Activated Carbon by One-Step Calcination of Deoxygenated Agar for High Voltage Lithium Ion Supercapacitor. *ACS Sustain. Chem. Eng.* **2020**, *8* (9), 3637–3643. https://doi.org/10.1021/acssuschemeng.9b06347.

(26) Wang, Q.; Ma, W.; Yin, E.; Yu, S.; Wang, S.; Xiang, H.; Li, D.; Zhu, M. Melt Spinning of Low-Cost Activated Carbon Fiber with a Tunable Pore Structure for High-Performance Flexible Supercapacitors. *ACS Appl. Energy Mater.* **2020**, *3* (9), 9360–9368. https://doi.org/10.1021/acsaem.0c01723.

(27) Chen, B. C.; Tsai, C. Y.; Pan, S. Y.; Chen, Y. T.; Hsi, H. C. Sustainable Recovery of Gaseous Mercury by Adsorption and Electrothermal Desorption Using Activated Carbon Fiber Cloth. *Environ. Sci. Technol.* **2020**, *54* (3), 1857–1866. https://doi.org/10.1021/acs.est.9b05114.

(28) Wang, F.; Tan, S.; Cao, Y.; Wang, D.; Wu, J.; Luo, F.; Liu, Q.; Xie, X.; Li, S.; Zhou, M. Experimental Study on the Influence of Surface Characteristics of Activated Carbon on Mercury Removal in Flue Gas. *Energy and Fuels* **2020**, *34* (5), 6168–6177. https://doi.org/10.1021/acs.energyfuels.0c00611.

(29) Lütke, S. F.; Igansi, A. V.; Pegoraro, L.; Dotto, G. L.; Pinto, L. A. A.; Cadaval, T. R. S. Preparation of Activated Carbon from Black Wattle Bark Waste and Its Application for Phenol Adsorption. *J. Environ. Chem. Eng.* **2019**, *7* (5), 103396. https://doi.org/10.1016/j.jece.2019.103396.

(30) Abdulrasheed, A. A.; Jalil, A. A.; Triwahyono, S.; Zaini, M. A. A.; Gambo, Y.; Ibrahim, M. Surface Modification of Activated Carbon for Adsorption of SO2 and NOX: A Review of Existing and Emerging Technologies. *Renewable and Sustainable Energy Reviews*. Elsevier Ltd October 1, 2018, pp 1067–1085. https://doi.org/10.1016/j.rser.2018.07.011.

(31) Li, L.; Liu, S.; Liu, J. Surface Modification of Coconut Shell Based Activated Carbon for the Improvement of Hydrophobic VOC Removal. *J. Hazard. Mater.* **2011**, *192* (2), 683–690. https://doi.org/10.1016/j.jhazmat.2011.05.069.

(32) Berber, M. R. Surface-functionalization of Activated Carbon with Polyglucosamine Polymer for Efficient Removal of Cadmium Ions. *Polym. Compos.* **2020**, *41* (8), 3074–3086. https://doi.org/10.1002/pc.25599.

(33) Azhagapillai, P.; Al Shoaibi, A.; Chandrasekar, S. Surface Functionalization Methodologies on Activated Carbons and Their Benzene Adsorption. *Carbon Lett.*

2020, *1*, 3. https://doi.org/10.1007/s42823-020-00170-w.

(34) Xing, W.; Wu, Y.; Li, C.; Lu, J.; Lin, X.; Yu, C. Biomass Activated Carbon/SiO2-Based Imprinted Membranes for Selective Separation of Atrazine: A Synergistic Integration System. *ACS Sustain. Chem. Eng.* **2020**, *8* (14), 5636–5647. https://doi.org/10.1021/acssuschemeng.0c00232.

(35) Wu, J. M.; Zhao, Q. E. Activation of Carbon Cloth and Concurrent Precipitation of Titania Nanowires for Enhanced Adsorption and Photocatalysis Performance. *Appl. Surf. Sci.* **2020**, *527*, 146779. https://doi.org/10.1016/j.apsusc.2020.146779.

(36) Li, X.; Zhang, L.; Yang, Z.; He, Z.; Wang, P.; Yan, Y.; Ran, J. Hydrophobic Modified Activated Carbon Using PDMS for the Adsorption of VOCs in Humid Condition. *Sep. Purif. Technol.* **2020**, *239*, 116517. https://doi.org/10.1016/j.seppur.2020.116517.

(37) Yoshikawa, Y.; Teshima, K.; Futamura, R.; Tanaka, H.; Iiyama, T.; Kaneko, K. Structural Adsorption Mechanism of Chloroform in Narrow Micropores of Pitch-Based Activated Carbon Fibres. *Carbon N. Y.* **2021**, *171*, 681–688. https://doi.org/10.1016/j.carbon.2020.08.020.

(38) Yang, K.; Pan, T.; Zhao, Q.; Chen, C.; Zhu, X.; Wang, P.; Chen, B. Dual-Function Ultrafiltration Membrane Constructed from Pure Activated Carbon Particles via Facile Nanostructure Reconstruction for High-Efficient Water Purification. *Carbon N. Y.* **2020**, *168*, 254–263. https://doi.org/10.1016/j.carbon.2020.06.083.

(39) Babu, C. M.; Binnemans, K.; Roosen, J. Ethylenediaminetriacetic Acid-Functionalized Activated Carbon for the Adsorption of Rare Earths from Aqueous Solutions. *Ind. Eng. Chem. Res.* **2018**, *57* (5), 1487–1497. https://doi.org/10.1021/acs.iecr.7b04274.

(40) Kostoglou, N.; Koczwara, C.; Prehal, C.; Terziyska, V.; Babic, B.; Matovic, B.; Constantinides, G.; Tampaxis, C.; Charalambopoulou, G.; Steriotis, T.; Hinder, S.; Baker, M.; Polychronopoulou, K.; Doumanidis, C.; Paris, O.; Mitterer, C.; Rebholz, C. Nanoporous Activated Carbon Cloth as a Versatile Material for Hydrogen Adsorption, Selective Gas Separation and Electrochemical Energy Storage. *Nano Energy* **2017**, *40*, 49–64. https://doi.org/10.1016/j.nanoen.2017.07.056.

(41) Polovina, M.; Babić, B.; Kaluderović, B.; Dekanski, A. Surface Characterization of Oxidized Activated Carbon Cloth. *Carbon N. Y.* **1997**, *35* (8), 1047–1052. https://doi.org/10.1016/S0008-6223(97)00057-2.

(42) Babić, B. M.; Milonjić, S. K.; Polovina, M. J.; Kaludierović, B. V. Point of Zero Charge and Intrinsic Equilibrium Constants of Activated Carbon Cloth. *Carbon N. Y.* **1999**, *37* (3), 477–481. https://doi.org/10.1016/S0008-6223(98)00216-4.

(43) Dantas, S.; Struckhoff, K. C.; Thommes, M.; Neimark, A. V. Pore Size Characterization of Micro-Mesoporous Carbons Using CO2 Adsorption. *Carbon N. Y.* **2021**, *173*, 842–848. https://doi.org/10.1016/J.CARBON.2020.11.059.

(44) Seo, Y. D.; Lee, C.; Lee, K. J.; Jang, J. Fabrication of Silica Nanotubes with an Anisotropic Functionality as a Smart Catalyst Supporter. *Chem. Commun.* **2016**, *52* (63), 9825–9828. https://doi.org/10.1039/c6cc02225a.

(45) Shi, L.; Hu, J.; Lin, X. D.; Fang, L.; Wu, F.; Xie, J.; Meng, F. M. A Robust Superhydrophobic PPS-PTFE/SiO2 Composite Coating on AZ31 Mg Alloy with Excellent Wear and Corrosion Resistance Properties. *J. Alloys Compd.* **2017**, *721*,

157–163. https://doi.org/10.1016/j.jallcom.2017.05.333.

(46) Guo, Y.; Zhao, E.; Guo, X.; Tang, D. Fabrication of Self-Assembled Hydrophobic Fluorinated Silica Particulate Film. *J. Fluor. Chem.* **2019**, *218*, 27–35. https://doi.org/10.1016/j.jfluchem.2018.11.013.

(47) Khan, S. A.; Zulfiqar, U.; Hussain, S. Z.; Zaheer, U.; Hussain, I.; Husain, S. W.; Subhani, T. Fabrication of Superhydrophobic Filter Paper and Foam for Oil–Water Separation Based on Silica Nanoparticles from Sodium Silicate. *J. Sol-Gel Sci. Technol.* **2016**, 1–9. https://doi.org/10.1007/s10971-016-4250-6.

(48) Zulfiqar, U.; Subhani, T.; Wilayat Husain, S. Towards Tunable Size of Silica Particles from Rice Husk. *J. Non. Cryst. Solids* **2015**, *429*. https://doi.org/10.1016/j.jnoncrysol.2015.08.037.

(49) Hu, L.; Zhang, S.; Zhang, Y.; Li, B. A Flexible Nanofiber-Based Membrane with Superhydrophobic Pinning Properties. *J. Colloid Interface Sci.* **2016**, *472*, 167–172. https://doi.org/10.1016/j.jcis.2016.03.056.

(50) Zha, J.; Ali, S. S.; Peyroux, J.; Batisse, N.; Claves, D.; Dubois, M.; Kharitonov, A. P.; Monier, G.; Darmanin, T.; Guittard, F.; Alekseiko, L. N. Superhydrophobicity of Polymer Films via Fluorine Atoms Covalent Attachment and Surface Nano-Texturing. *J. Fluor. Chem.* **2017**, *200*, 123–132. https://doi.org/10.1016/j.jfluchem.2017.06.011.

(51) Zhan, C.; Yu, X.; Liang, Q.; Liu, W.; Wang, Y.; Lv, R.; Huang, Z. H.; Kang, F. Flour Food Waste Derived Activated Carbon for High-Performance Supercapacitors. *RSC Adv.* **2016**, *6* (92), 89391–89396. https://doi.org/10.1039/c6ra18056f.

(52) Yang, C.; Jing, X.; Wang, F.; Ehmann, K. F.; Tian, Y.; Pu, Z. Fabrication of Controllable Wettability of Crystalline Silicon Surfaces by Laser Surface Texturing and Silanization. *Appl. Surf. Sci.* **2019**, *497*, 143805. https://doi.org/10.1016/j.apsusc.2019.143805.

(53) Li, M.; Huang, X.; Luo, W.; Chen, Y.; Han, F.; Cheng, X. Thermal Degradation Behavior of Self-Assembled Monolayer Surfactant on Silicon Substrate. *J. Vac. Sci. Technol. B* **2020**, *38* (3), 032602. https://doi.org/10.1116/1.5143307.

(54) Ferrari, A.; Robertson, J. Interpretation of Raman Spectra of Disordered and Amorphous Carbon. *Phys. Rev. B - Condens. Matter Mater. Phys.* **2000**, *61* (20), 14095–14107. https://doi.org/10.1103/PhysRevB.61.14095.

(55) Keppetipola, N. M.; Dissanayake, M.; Dissanayake, P.; Karunarathne, B.; Dourges, M. A.; Talaga, D.; Servant, L.; Olivier, C.; Toupance, T.; Uchida, S.; Tennakone, K.; Kumara, G. R. A.; Cojocaru, L. Graphite-Type Activated Carbon from Coconut Shell: A Natural Source for Eco-Friendly Non-Volatile Storage Devices. *RSC Adv.* **2021**, *11* (5), 2854–2865. https://doi.org/10.1039/d0ra09182k.

(56) Liu, D.; Xu, B.; Zhu, J.; Tang, S.; Xu, F.; Li, S.; Jia, B.; Chen, G. Preparation of Highly Porous Graphitic Activated Carbon as Electrode Materials for Supercapacitors by Hydrothermal Pretreatment-Assisted Chemical Activation. *ACS Omega* **2020**, *5* (19), 11058–11067. https://doi.org/10.1021/acsomega.0c00938.

(57) Xie, X. B.; Wu, D.; Wu, H.; Hou, C.; Sun, X.; Zhang, Y.; Yu, R.; Zhang, S.; Wang, B.; Du, W. Dielectric Parameters of Activated Carbon Derived from Rosewood and Corncob. *J. Mater. Sci. Mater. Electron.* **2020**, *31* (20), 18077–18084.

https://doi.org/10.1007/s10854-020-04358-8.

(58) Li, Z. Q.; Lu, C. J.; Xia, Z. P.; Zhou, Y.; Luo, Z. X-Ray Diffraction Patterns of Graphite and Turbostratic Carbon. *Carbon N. Y.* **2007**, *45* (8), 1686–1695. https://doi.org/10.1016/j.carbon.2007.03.038.

(59) Kitzmann, J.; Göritz, A.; Fraschke, M.; Lukosius, M.; Wenger, C.; Wolff, A.; Lupina, G. Perfluorodecyltrichlorosilane-Based Seed-Layer for Improved Chemical Vapour Deposition of Ultrathin Hafnium Dioxide Films on Graphene. *Sci. Rep.* **2016**, *6* (1), 1–6. https://doi.org/10.1038/srep29223.

(60) Tang, M. M.; Bacon, R. Carbonization of Cellulose Fibers-I. Low Temperature Pyrolysis. *Carbon N. Y.* **1964**, *2* (3), 211–220. https://doi.org/10.1016/0008-6223(64)90035-1.

(61) Bacon, R.; Tang, M. M. Carbonization of Cellulose Fibers-II. Physical Property Study. *Carbon N. Y.* **1964**, *2* (3), 221–225. https://doi.org/10.1016/0008-6223(64)90036-3.

(62) Gao, Y.; Yue, Q.; Gao, B.; Li, A. Insight into Activated Carbon from Different Kinds of Chemical Activating Agents: A Review. *Science of the Total Environment*. Elsevier B.V. December 1, 2020, p 141094. https://doi.org/10.1016/j.scitotenv.2020.141094.

(63) Qian, F.; Zhu, X.; Liu, Y.; Hao, S.; Ren, Z. J.; Gao, B.; Zong, R.; Zhang, S.; Chen, J. Synthesis, Characterization and Adsorption Capacity of Magnetic Carbon Composites Activated by CO2: Implication for the Catalytic Mechanisms of Iron Salts. *J. Mater. Chem. A* **2016**, *4* (48), 18942–18951. https://doi.org/10.1039/c6ta06614c.

(64) Nowrouzi, M.; Behin, J.; Younesi, H.; Bahramifar, N.; Charpentier, P. A.; Rohani, S. An Enhanced Counter-Current Approach towards Activated Carbon from Waste Tissue with Zero Liquid Discharge. *Chem. Eng. J.* **2017**, *326*, 934–944. https://doi.org/10.1016/j.cej.2017.05.141.

(65) Sternik, D.; Wiśniewska, M.; Nowicki, P. Thermal Degradation of Peat-Based Activated Carbons Covered with Mixed Adsorption Layers of PAA Polymer and SDS Surfactant. *Thermochim. Acta* **2019**, *676*, 71–83. https://doi.org/10.1016/j.tca.2019.03.039.

(66) Pang, B.; Liu, H.; Liu, P.; Zhang, H.; Avramidis, G.; Chen, L.; Deng, X.; Viöl, W.; Zhang, K. Robust, Easy-Cleaning Superhydrophobic/Superoleophilic Copper Meshes for Oil/Water Separation under Harsh Conditions. *Adv. Mater. Interfaces* **2019**, *6* (11), 1900158. https://doi.org/10.1002/admi.201900158.

(67) Han, L.; Bi, H.; Xie, X.; Su, S.; Mao, P.; Sun, L. Superhydrophobic Graphene-Coated Sponge with Microcavities for High Efficiency Oil-in-Water Emulsion Separation. *Nanoscale* **2020**, *12* (34), 17812–17820. https://doi.org/10.1039/d0nr04892e.